symmetry

MDPI

Article

Ferrohydrodynamic and Magnetohydrodynamic Effects on Jet Flow and Heat Transfer of Fe_3O_4-H_2O Nanofluid in a Microchannel Subjected to Permanent Magnets

Yunfeng Xie, Changwei Jiang *, Peijia Zheng, Zhichao Cao and Minghong Luo

School of Energy and Power Engineering, Changsha University of Science and Technology, Changsha 410004, China; XYF13687382460@163.com (Y.X.); zpj19940408@163.com (P.Z.); c15116285887@126.com (Z.C.); cslg_std_lm1027@163.com (M.L.)
* Correspondence: jiangcw@csust.edu.cn; Tel.: +86-73185258409

Abstract: In the present study, the two-dimensional jet flow of Fe_3O_4-H_2O nanofluid was numerically investigated in a microchannel. The main objective of this article was to study the impact of permanent magnets on both ferromagnetic hydrodynamic and thermal behavior. A ferromagnetic hydrodynamic model, which includes the Brown effect and thermophoretic effect, was applied to simulate the problem through solving momentum, energy, and volume fraction equations. In this regard, different results, including the velocity vector, temperature distribution, and Nusselt number, were analyzed. Moreover, the influence of Kelvin force, inlet opening, permanent magnets position, and Reynolds number were studied on the jet flow and heat transfer. The obtained results demonstrate these factors significantly affect the jet flow and heat transfer of Fe_3O_4-H_2O nanofluid in the microchannel. Moreover, it was found that the magnetic field originating from permanent magnets can effectively solve the problem of local high temperature on the wall at low inlet opening. The heat transfer gain was the most obvious when the position of the permanent magnet was close to the microchannel entrance. When inlet opening and permanent magnets position are 1/4 and 1, respectively, the heat transfer gain was largest, reaching 35.2%.

Keywords: nanofluid; ferromagnetic hydrodynamics (FHD); numerical simulation; jet flow; heat transfer

Citation: Xie, Y.; Jiang, C.; Zheng, P.; Cao, Z.; Luo, M. Ferrohydrodynamic and Magnetohydrodynamic Effects on Jet Flow and Heat Transfer of Fe_3O_4-H_2O Nanofluid in a Microchannel Subjected to Permanent Magnets. *Symmetry* **2021**, *13*, 2051. https://doi.org/10.3390/sym13112051

Academic Editor: Alexander Zlotnik

Received: 12 October 2021
Accepted: 29 October 2021
Published: 31 October 2021

1. Introduction

With the rapid development of microelectronics technology, the increasing heat flux puts forward higher requirements to dissipate the generated heat in electronic equipment [1,2]. In this regard, different technologies such as installing the fins, adding phase change materials were put forward [3,4].

In recent years, with the development of nanotechnology, nanofluid can be used in the field of heat transfer enhancement [5]. Nanofluid is a stable suspension composed of base fluid and nanoparticles. The purpose of adding nanoparticles is to improve the thermophysical properties of base fluid, which makes nanofluid attractive and widely used in different applications, including thermal engineering, bioengineering, and electronic industry [6,7].

Buongiorno et al. [8] considered the sliding velocity between nanoparticles and fluid and proposed a non-uniform model in this regard. They showed that the particle velocity was mainly affected by the thermophoresis effect and Brownian motion. Meanwhile, the magnetic field is an effective way to control the motion of nanoparticles by balancing these effects. Corcione et al. [9] proposed empirical expressions to calculate effective thermal conductivity and dynamic viscosity of nanofluid. It was found that the ratio of thermal conductivity of nanofluid to that of the base fluid increases has a direct correlation with the volume fraction, temperature, and diameter of nanoparticles.

In addition to improving the calculation model, the researchers also studied the influence of jet, nanofluid type, volume fraction, and diameter of nanoparticles on the heat transfer. Moreover, Ekiciler et al. [10] conducted numerical studies on heat transfer and entropy generation of Al_2O_3-water nanofluids with different shapes of nanoparticles. The results show that the heat transfer rate increases with the increase of the volume fraction of nanoparticles. Ambreen et al. [11] proposed a discrete phase model to study the effect of particle size on the pressure drop and forced convection heat transfer in a microchannel. Bowers et al. [12] performed experiments and studied the heat transfer of Al_2O_3 nanofluid in the microchannel. The obtained results showed that the flow rate of nanofluid and the volume fraction of nanoparticles have important effects on the heat transfer in the microchannel. Vijayan et al. [13] analyzed the thermal characteristics of an unshielded receiver tube of an integrated solar parabolic with a low volume fraction Al_2O_3 and deionized water nanofluid as the heat transfer. Kaya et al. [14] numerically studied the forced convective flow and heat transfer characteristics of TiO_2-H_2O nanofluids with different volume fractions in semicircular cross-section microchannels.

Recently, a magnetic field has been widely applied to improve the heat transfer of nanofluid. Sheikholeslami et al. [15,16] used the Lattice Boltzmann method to simulate the magnetic fluid flowing under the action of the magnetic field in a complex spatial structure. The results show that when the magnetic field is along the magnetic fluid, the heat transfer effect is significantly enhanced. Karami et al. [17] investigated the impact of volume fraction on the convective heat transfer of a nanofluid in a microchannel under static and rotating magnetic fields. Mixed convective heat transfer and natural convection heat transfer in a porous cavity subjected to the magnetic field were examined numerically by Cunha et al. [18–20]. Salehpour et al. [21–23] studied the MHD heat transfer in rectangular porous channels subjected to constant and alternating magnetic fields and analyzed the influence of frequency on heat transfer rate and pressure drop. It was found that the alternating magnetic field reduces the pressure drop and improves the heat transfer in the channel. Mehrez et al. [24] numerically studied the heat transfer and flow behavior of Fe_3O_4-water nanofluids in horizontal channels under a magnetic field. Larimi et al. [25] investigated the influence of different configurations of the magnetic field on the heat transfer, pressure loss, wall shear stress of the channel. Bagherzadeh et al. [26–28] performed numerical simulations and studied the influence of cavity shape on thermomagnetic convection of nanofluid subjected to the magnetic field by changing the shape of the closed channel. Sivasankaran et al. [29] carried out numerical simulations and investigated the effects of the channel size and Hartmann number on the heat transfer and fluid flow characteristics of trapezoidal microchannel heat sink under the magnetic field, and found that the thermomagnetic convection can enhance convective heat transfer. Zanella et al. [30] innovatively studied the influence of magnetic core structure and magnetic field intensity on the thermal magnetic convection by setting a magnetic core in the channel. Considering the Brownian diffusion, thermophoresis, and magnetophoresis. Soltanipour et al. [31] applied a two-phase model to investigate the forced convection of Fe_3O_4-H_2O magnetic nanofluid in a heated tube subjected to a quadrupole magnetic field.

Most research focuses on the thermomagnetic convection of nanofluid subjected to a magnetic dipole or a uniform magnetic field, which is difficult to implement in practical applications, but it is convenient to implement engineering applications by using a magnet to generate the magnetic field. Microchannels are often used for heat dissipation in electronic and microelectronic equipment. At present, there are few studies on the effect of permanent magnets on the heat transfer of nanofluids in the microchannel. The current work investigates the jet flow and heat transfer of Fe_3O_4-H_2O nanofluid under the conditions of symmetrical microchannel geometry, symmetrical heat flux boundary, and symmetrical magnet arrangement, and the effects of the inlet opening, Reynolds number, and magnet position on flow and heat transfer characteristics are analyzed.

2. Physical and Mathematical Model

2.1. Problem Description

The physical model was simplified from the chip's three-dimensional stacking system. The physical model and coordinate system are shown in Figure 1, indicating that the height and length of two-dimensional plane microchannel are h = 2 mm and l = 20 mm, respectively. Fe_3O_4-H_2O nanofluid enters the microchannel in the form of a jet with an inlet width of d. It should be indicated that nanoparticles have uniform temperature, velocity, and volume fraction distributions at the inlet of the microchannel. The thermophysical characteristics of the Fe_3O_4-H_2O nanofluid are shown in Table 1. Moreover, the same constant heat flux q is applied to the upper and lower walls of the microchannel while the side walls are insulated. Two identical permanent magnets are symmetrically arranged on both sides of the microchannel. The length l_1 and width h_1 of the permanent magnet is 0.5 mm and 1 mm, respectively, the longitudinal distance between the magnet and the wall surface h_2 is 1 mm. The distance between magnets and microchannel entrance is x_i.

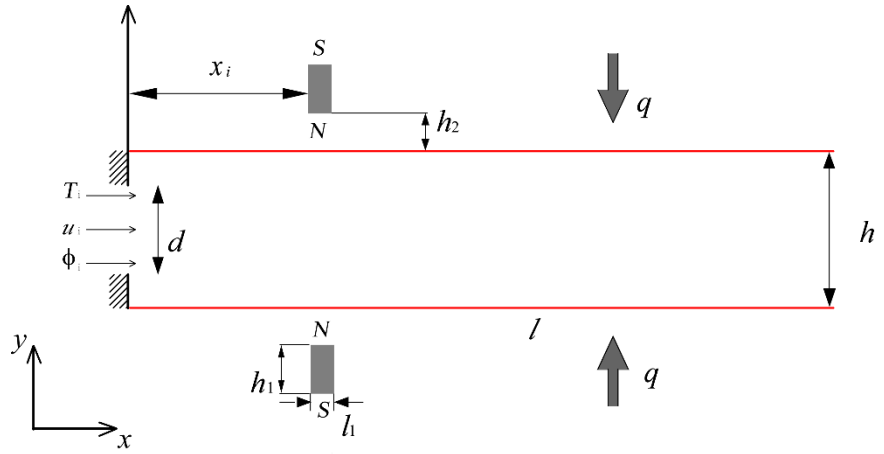

Figure 1. Configuration of the established model.

Table 1. Thermophysical characteristics of water and Fe_3O_4 nanoparticles [32].

	C_p (J/kg·K)	ρ (kg/m^3)	k (W/m·K)	μ (N·s/m^2)	β (1/K)
H_2O	4179	997.1	0.613	0.001	1.8×10^{-3}
Fe_3O_4	670	5200	6	0	0

2.2. Governing Equations

The Fe_3O_4-H_2O nanofluid is electrically non-conductive. Accordingly, there is no free electromagnetic current in the flow. The magnetic field induced by permanent magnets follows the following Maxwell's equation:

$$\nabla \cdot \mathbf{B} = 0 \tag{1}$$

$$\nabla \times \mathbf{H} = 0 \tag{2}$$

where the following correlation exists between **B** and **H**:

$$\mathbf{B} = \mu_0(1+\chi)\mathbf{H} \tag{3}$$

Based on the Buongiorno model, considering the Brown effect and thermophoretic effect, the conservation equations are as follows [32]:

mass equation:

$$\frac{\partial u}{\partial x} + \frac{\partial v}{\partial y} = 0 \tag{4}$$

momentum equations:

$$\begin{aligned}\rho_{nf}(u\tfrac{\partial u}{\partial x}+v\tfrac{\partial u}{\partial y}) &= -\tfrac{\partial p^*}{\partial x}+\mu_{nf}(\tfrac{\partial^2 u}{\partial x^2}+\tfrac{\partial^2 u}{\partial y^2})-\tfrac{1}{2}\mu_0\chi_0\beta_{nf}(T-T_i)\tfrac{\partial \mathbf{H}^2}{\partial x}\\ &-\mu_0\chi_0^2\beta_{nf}(T-T_i)\tfrac{\partial \mathbf{H}^2}{\partial x}-\mu_0\chi_0^2\beta_{nf}\left(H_x\tfrac{\partial T}{\partial x}+H_y\tfrac{\partial T}{\partial y}\right)H_x\end{aligned} \tag{5}$$

$$\begin{aligned}\rho_{nf}(u\tfrac{\partial v}{\partial x}+v\tfrac{\partial v}{\partial y}) &= -\tfrac{\partial p^*}{\partial y}+\mu_{nf}\left(\tfrac{\partial^2 v}{\partial x^2}+\tfrac{\partial^2 v}{\partial y^2}\right)-\tfrac{1}{2}\mu_0\chi_0\beta_{nf}(T-T_i)\tfrac{\partial \mathbf{H}^2}{\partial y}\\ &-\mu_0\chi_0^2\beta_{nf}(T-T_i)\tfrac{\partial \mathbf{H}^2}{\partial y}-\mu_0\chi_0^2\beta_{nf}\left(H_x\tfrac{\partial T}{\partial x}+H_y\tfrac{\partial T}{\partial y}\right)H_y\end{aligned} \tag{6}$$

energy equation:

$$\begin{aligned}(\rho C_p)_{nf}\left(u\tfrac{\partial T}{\partial x}+v\tfrac{\partial T}{\partial y}\right) &= k_{nf}\left(\tfrac{\partial^2 T}{\partial x^2}+\tfrac{\partial^2 T}{\partial y^2}\right)+\\ (\rho C_p)_p\left(D_B\left(\tfrac{\partial \phi}{\partial x}\tfrac{\partial T}{\partial x}+\tfrac{\partial \phi}{\partial y}\tfrac{\partial T}{\partial y}\right)+\tfrac{D_T}{T_i}\left(\left(\tfrac{\partial T}{\partial x}\right)^2+\left(\tfrac{\partial T}{\partial y}\right)^2\right)\right)\end{aligned} \tag{7}$$

volume fraction equation:

$$\left(u\frac{\partial \phi}{\partial x}+v\frac{\partial \phi}{\partial y}\right) = D_B\left(\frac{\partial^2 \phi}{\partial x^2}+\frac{\partial^2 \phi}{\partial y^2}\right)+\frac{D_T}{T_i}\left(\frac{\partial^2 T}{\partial x^2}+\frac{\partial^2 T}{\partial y^2}\right) \tag{8}$$

where $p^* = p-\mu_0\chi_0(1+\chi_0)\mathbf{H}^2/2$ is the magnetostatic pressure.

The specific deduction process of momentum equations is discussed in Appendix A. ρ_{nf}, $(\rho C_p)_{nf}$, β_{nf} of Fe_3O_4-H_2O nanofluid are defined as:

$$\rho_{nf} = (1-\phi)\rho_f+\phi\rho_p \tag{9}$$

$$(\rho C_p)_{nf} = (1-\phi)(\rho C_p)_f+\phi(\rho C_p)_p \tag{10}$$

$$\beta_{nf} = (1-\phi)\beta_f+\phi\beta_p \tag{11}$$

D_B and D_T are given by [32]:

$$D_B = \frac{k_B T}{3\pi\mu_f d_p} \tag{12}$$

$$D_T = 0.26\frac{k_f}{2k_f+k_p}\frac{\mu_f}{\rho_f}\phi \tag{13}$$

In the present study, the Corcione model was applied to calculate the viscosity and thermal conductivity. This model can be mathematically expressed as follows [9]:

$$\mu_{nf} = \frac{\mu_f}{1-34.87(d_p/d_f)^{-0.3}\phi^{1.03}} \tag{14}$$

$$\frac{k_{nf}}{k_f} = 1+4.4Re_B^{0.4}Pr^{0.66}\left(\frac{T}{T_{fr}}\right)^{10}\left(\frac{k_p}{k_f}\right)^{0.03}\phi^{0.66} \tag{15}$$

$$Re_B = \frac{\rho_f d_p}{\mu_f}\frac{2k_B T}{\pi\mu d_p^2} \tag{16}$$

The boundary conditions of the inlet (jet and wall), outlet, lower and upper walls are in the form below:

inlet:

$$u = u_i, v = 0, T = T_i, \phi = \phi_i \tag{17a}$$

$$u = v = 0, \frac{\partial T}{\partial x} = \frac{\partial \phi}{\partial x} = 0 \tag{17b}$$

outlet:

$$p = 0, \frac{\partial T}{\partial x} = \frac{\partial \phi}{\partial x} = 0 \tag{18}$$

lower and upper walls:

$$u = v = 0, \frac{\partial T}{\partial y}\Big|_{y=0} = \frac{q}{k_{nf}}, \frac{\partial T}{\partial y}\Big|_{y=h} = -\frac{q}{k_{nf}}, D_B \frac{\partial \phi}{\partial y} + \frac{D_T}{T_i}\frac{\partial T}{\partial y} = 0 \tag{19}$$

In order to obtain non-dimensional equations, the following definitions are provided:

$(X, Y) = \frac{(x,y)}{h}$; $(U, V) = \frac{(u,v)}{u_i}$; $P = \frac{p^*}{\rho_{nf} u_i^2}$; $\theta = \frac{T - T_i}{qh/k_f}$; $\varphi = \frac{\phi}{\phi_i}$; $\overline{\mathbf{H}} = \frac{\mu_0 \mathbf{H}}{Br}$; $R = \frac{d}{h}$;

$Re = \frac{u_i d \rho_f}{\mu_f}$; $Le = \frac{k_f}{D_B (\rho C p)_f}$; $N_B = D_B \frac{(\rho C_p)_p}{k_f} \phi_i$; $N_T = D_T \frac{(\rho C_p)_p}{k_f} \frac{qh}{k_f}$; $\gamma = \frac{\chi_0 \beta_{nf} q h B r^2}{\mu_0 \rho_{nf} k_{nf} u_i^2}$

The dimensionless form of the governing equation is as follows:

$$\frac{\partial U}{\partial X} + \frac{\partial V}{\partial Y} = 0 \tag{20}$$

$$\begin{aligned} U\frac{\partial U}{\partial X} + V\frac{\partial U}{\partial Y} &= -\frac{\partial P}{\partial X} + \frac{R}{Re}\frac{\rho_f}{\rho_{nf}}\frac{\mu_{nf}}{\mu_f}\left(\frac{\partial^2 U}{\partial X^2} + \frac{\partial^2 U}{\partial Y^2}\right) - \frac{1}{2}\gamma\theta\frac{\partial \overline{\mathbf{H}}^2}{\partial X} \\ &-\chi_0\gamma\theta\frac{\partial \overline{\mathbf{H}}^2}{\partial X} - \chi_0\gamma\left(\overline{H}_X\frac{\partial \theta}{\partial X} + \overline{H}_Y\frac{\partial \theta}{\partial Y}\right)\overline{H}_X \end{aligned} \tag{21}$$

$$\begin{aligned} U\frac{\partial V}{\partial X} + V\frac{\partial V}{\partial Y} &= -\frac{\partial P}{\partial Y} + \frac{R}{Re}\frac{\rho_f}{\rho_{nf}}\frac{\mu_{nf}}{\mu_f}\left(\frac{\partial^2 V}{\partial X^2} + \frac{\partial^2 V}{\partial Y^2}\right) - \frac{1}{2}\gamma\theta\frac{\partial \overline{\mathbf{H}}^2}{\partial Y} \\ &-\chi_0\gamma\theta\frac{\partial \overline{\mathbf{H}}^2}{\partial Y} - \chi_0\gamma\left(\overline{H}_X\frac{\partial \theta}{\partial X} + \overline{H}_Y\frac{\partial \theta}{\partial Y}\right)\overline{H}_Y \end{aligned} \tag{22}$$

$$\begin{aligned} U\frac{\partial \theta}{\partial X} + V\frac{\partial \theta}{\partial Y} &= \frac{R}{RePr}\frac{(\rho C_p)_f}{(\rho C_p)_{nf}}\frac{k_{nf}}{k_f}\left(\frac{\partial^2 \theta}{\partial X^2} + \frac{\partial^2 \theta}{\partial Y^2}\right) + \\ &\frac{R}{RePr}\frac{(\rho C_p)_f}{(\rho C_p)_{nf}}\left[N_B\left(\frac{\partial \varphi}{\partial X}\frac{\partial \theta}{\partial X} + \frac{\partial \varphi}{\partial Y}\frac{\partial \theta}{\partial Y}\right) + N_T\left(\left(\frac{\partial \theta}{\partial X}\right)^2 + \left(\frac{\partial \theta}{\partial Y}\right)^2\right)\right] \end{aligned} \tag{23}$$

$$U\frac{\partial \varphi}{\partial X} + V\frac{\partial \varphi}{\partial Y} = \frac{R}{RePrLe}\left(\frac{\partial^2 \varphi}{\partial X^2} + \frac{\partial^2 \varphi}{\partial Y^2}\right) + \frac{R}{RePrLe}\frac{N_T}{N_B}\left(\frac{\partial^2 \theta}{\partial X^2} + \frac{\partial^2 \theta}{\partial Y^2}\right) \tag{24}$$

Equations (20–24) are subjected to the following boundary conditions.

inlet:

$$U = 1, V = 0, \theta = 0, \varphi = 1 \tag{25a}$$

$$U = V = 0, \frac{\partial \theta}{\partial X} = \frac{\partial \varphi}{\partial X} = 0 \tag{25b}$$

outlet:

$$P = 0, \frac{\partial \theta}{\partial X} = \frac{\partial \varphi}{\partial X} = 0 \tag{26}$$

lower and upper walls:

$$U = V = 0, \frac{\partial \theta}{\partial Y}|_{Y=0} = \frac{k_f}{k_{nf}}, \frac{\partial \theta}{\partial Y}|_{Y=1} = -\frac{k_f}{k_{nf}}, N_B\frac{\partial \varphi}{\partial Y} + N_T\frac{\partial \theta}{\partial Y} = 0 \tag{27}$$

The local and average Nusselt numbers of the upper wall can be obtained as follows:

$$Nu = \frac{qh}{k_f(T - T_i)} \tag{28}$$

$$Nu_{ave} = \frac{1}{L}\int_0^L Nu dX \tag{29}$$

2.3. Numerical Method

In this section, ANSYS software was applied to simulate the magnetic field and obtain a two-dimensional static magnetic field. Then the magnetic potential equation was combined with continuity, momentum, and energy conservation equations. Moreover, the finite volume method (FVM) was applied to solve equations. In this regard, convection and diffusion terms were discretized using third-order QUICK and second-order central difference schemes, respectively. Furthermore, the tridiagonal matrix algorithm (TDMA) and the successive over-relaxation (SOR) schemes were applied to solve the governing equations iteratively. Meanwhile, the SIMPLE algorithm was utilized to solve the pressure-velocity coupling. In all simulations, the maximum residue of 10^{-6} was considered as the convergence criterion.

2.4. Grid Independence Test

In order to perform the grid independence, different grid resolutions were considered for the case γ = 19.59 (Br = 2 T), Re = 11.8 and R = 1. In this regard, Table 2 presents the obtained average Nusselt number on the upper wall, indicating that the grid independency can be achieved for a 55 × 550 grid. Consequently, considering the calculation cost and accuracy, a grid-resolution of 55 × 550 was used in all calculations.

Table 2. The average Nusselt number on the upper wall with different grid numbers at Re = 47.2, R = 1, γ = 19.59.

Mesh Size	**20 × 200**	**40 × 400**	**45 × 450**	**50 × 500**	**55 × 550**
Nu_{ave}	4.506	4.416	4.410	4.405	4.403

To evaluate the accuracy of the numerical model, results issued by Ranjan et al. [33] were selected as the benchmark solution. In this regard, Figure 2 shows the temperature distribution and velocity vectors in the studied case. Table 3 compares the average Nusselt number of them, the maximum error between them was 3.13%. It was observed that the obtained results were in excellent agreement with those issued by Ranjan et al. [33], thereby validating the established model.

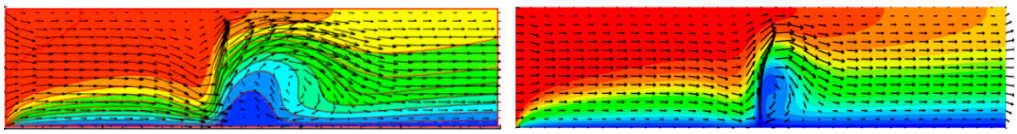

Figure 2. The temperature distribution and velocity vectors.

Table 3. Distribution of the Nusselt number.

***m* (A·m)**	Nu_{ave}		
	Ranjan et al. [33]	**Present Work**	**Relative Error/%**
0	2.610	2.603	−0.27
0.19	2.670	2.664	−0.22
0.58	2.880	2.890	0.35

3. Results and Discussion

Studies show that Fe_3O_4-H_2O nanofluid jet flow and convective heat transfer were affected by different parameters, including volume fraction (ϕ), inlet opening (R), Reynold number (Re), permanent magnet position (X_i), Kelvin force number (γ), and so on. In the present study, inlet temperature of nanofluid (T_i), heat flux (q), inlet volume fraction of nanofluid (ϕ_i), Kelvin force number (γ), magnetic susceptibility at reference temperature (χ_0) were kept constant at T_i = 293 K, q = 5 W/cm^2, ϕ_i = 0.05, γ = 19.59 (Br = 2 T), χ_0 = 0.06.

In this section, it is intended to focus on the influence of inlet opening (R), Reynolds number (Re), magnet position (X_i) on the jet flow, and heat transfer characteristics of nanofluid in the microchannel.

Figure 3 shows the magnetic flux density that is produced under permanent magnets along the X-axis centerline of the microchannel. It can be seen that the magnetic flux density curve presents an M-shaped distribution along the length of the microchannel. The magnetic flux density on both sides of the magnet was the largest, reaching 0.054 T, while the magnetic flux density under the magnet was the smallest, close to 0. The model equation includes the effect of Kelvin force, thermophoresis, and so on. Thus, the Fe_3O_4 nanoparticles in nanofluid will move along the gradient magnetic field under the action of Kelvin force generated by the gradient magnetic field, thus the Kelvin force near the two sides of the magnet was the largest. At the same time, the magnetization of Fe_3O_4 nanoparticles decreased significantly at high temperatures. Therefore, the effect of the gradient magnetic field on the flow and heat transfer performance of the nanofluid in the central region of the microchannel was greater than that in the region near the hot wall. In addition, the nanofluid will migrate to the lower temperature region because of thermophoresis, thus the magnetic field effect will be further enhanced in the low-temperature region. The local asymmetry of the thermal boundary layer around the magnet and the spatial heterogeneity of fluid sensitivity will lead to the flow of cold nanofluid near the magnet. The alternating decrease and increase of magnetization of magnetic particles will lead to the generation of the disturbed region near the magnet.

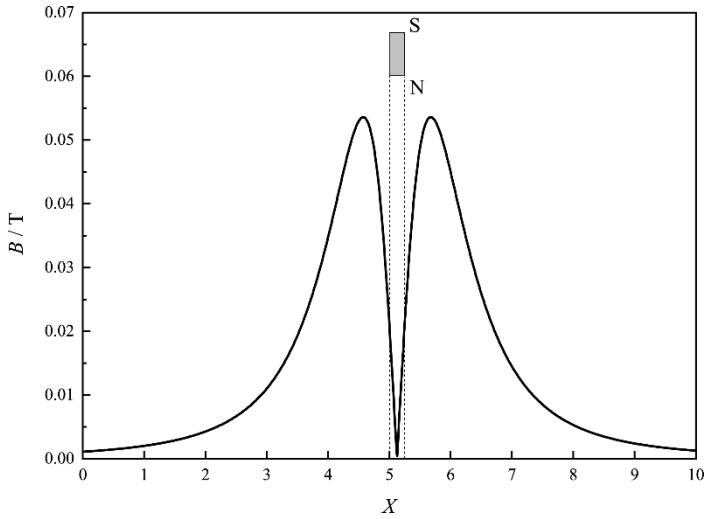

Figure 3. Magnetic flux density distribution along the X-axis centerline.

3.1. Effect of Inlet Opening (R)

The velocity vector and temperature distribution of nanofluid in the microchannel at various inlet openings when X_i = 4 and Re = 35.4 are presented in Figure 4. When the inlet opening is large, e.g., R = 1, 1/2, 1/4, the nanofluid in the microchannel is symmetrical up and down, and the streamline and isotherm are smooth. When the inlet opening is reduced to R = 1/8, the nanofluid flow deflects upward to form an asymmetric structure. When the inlet opening is reduced to R = 1/8, the nanofluid deflects upward to form an asymmetric structure. This is because the fluid enters the sudden expansion pipe at a low Reynolds number, the pipe diameter increases suddenly, the fluid flow state changes, and fluid flow forms turbulence. There are two recirculation zones near the upper and lower walls, and the local high temperature appears at the microchannel entrance. The local high-temperature region at the microchannel entrance increases with the decrease of the inlet opening.

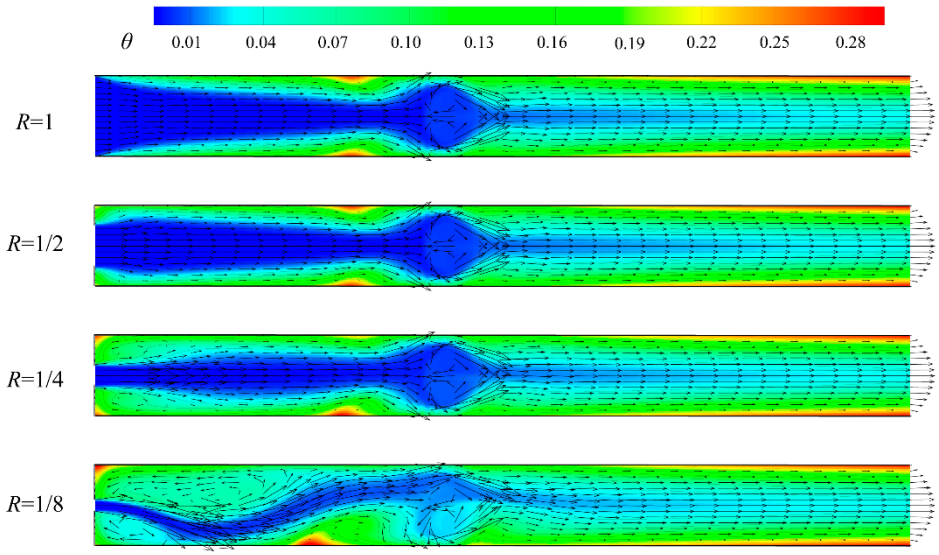

Figure 4. Effect of inlet opening on the velocity vector and temperature field in a microchannel for X_i = 4 and Re = 35.4.

Figure 5 shows the distribution of the temperature along the upper wall in the microchannel at various inlet openings when X_i = 4 and Re = 47.2. It can be seen that the wall temperature near the magnet decreased greatly, and the local high-temperature region was formed at the front end of the magnet due to the velocity stagnation. When the inlet opening decreases, the local high temperature appears in the entrance corner of the microchannel, and the local high temperature increases with the decreasing of the inlet opening. When R = 1/8, the velocity stagnation region at the front end of the magnet becomes the highest temperature region in the whole microchannel, which has an adverse effect on the overall heat transfer performance of the microchannel. Especially, the nanofluid near the magnetic pole is affected by the magnetic pole and forms a vortex, which destroys the fluid boundary layer on the wall near the magnetic pole. This results in a zigzag temperature distribution near the magnet pole.

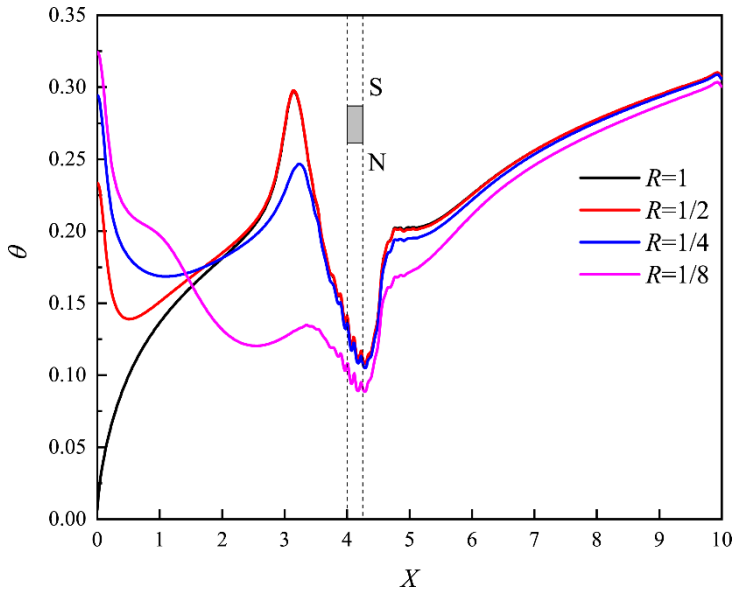

Figure 5. Effect of inlet opening on the temperature at the upper wall for X_i = 4 and Re = 47.2.

Figure 6 presents the Nu_{loc} at the upper wall in the microchannel at various inlet openings when X_i = 4 and Re = 47.2. In general, the magnetic field enhances nanofluid flow at different openings, the turbulent region near the magnet enhances the convective heat transfer, and Nu_{loc} at the entrance decreases with the increase of opening. When R = 1, it decreases along the flow direction of the nanofluid, and fluctuates obviously near the magnet, and then tends to be stable. This is because the magnetic particles in the nanofluid near the magnet move to the hot wall under the action of Kelvin force, which makes the local thermal conductivity increase and the local heat transfer ability increases. When R = 1/2 and R = 1/4, the Nu_{loc} at the upper wall is close. When R = 1/8, it increases gradually along the microchannel and reaches the maximum near the magnet. This is due to the upward deflection of the nanofluid jet after it hits the lower wall of the microchannel when the inlet opening is small, resulting in a counterclockwise vortex on the upper wall of the front end of the magnet, forming a stagnation region. The existence of the magnet makes this phenomenon more obvious, which leads to the gradual enhancement of heat transfer ability at the upper wall.

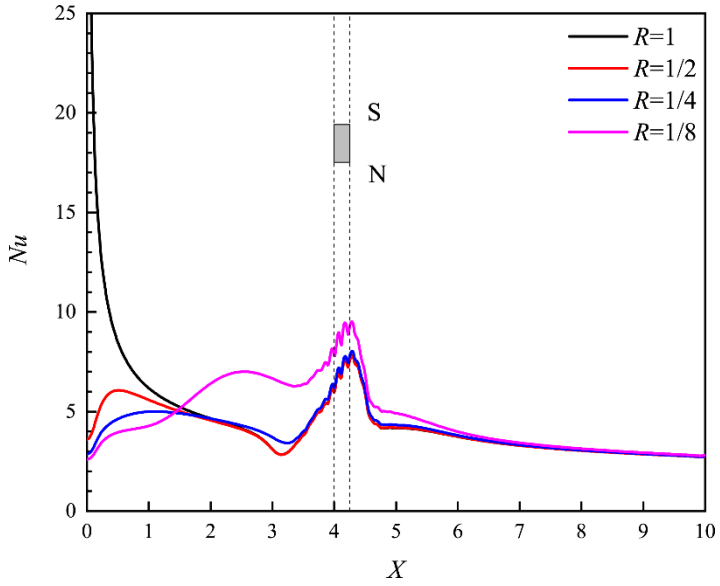

Figure 6. Effect of inlet opening on Nu_{loc} at the upper wall for X_i = 4 and Re = 47.2.

3.2. Effect of Reynold Number (Re)

Figure 7 illustrates the Nu_{loc} at the upper wall for various Reynolds numbers when X_i = 4 and R = 1/4. The influence of the magnetic field on high-speed nanofluid is greater than that on the low-speed nanofluid. Especially when Re > 70.0, the high-speed jet of nanofluid deflects upward, the Nu_{loc} of the upper wall at the microchannel entrance increases significantly, and the heat transfer performance at the upper wall increases significantly.

Figure 8 illustrates the velocity vector and temperature field in the microchannel at various magnet positions when R = 1 and Re = 47.2. The stagnation region of the front end of the magnet increases with the increase of the position. Under the action of Kelvin force, nanofluid first extrudes to the middle channel and then impacts the wall. In addition, the magnetic field intensity directly below the magnet is small, the temperature of magnetic particles moving near the wall increases, the magnetic intensity decreases, and the Kelvin force decreases, which causes the nanofluid to rebound and continue to squeeze toward the microchannel center after impacting the wall. The stagnation region of the front end of the magnet increases with the increase of X_i. When the magnet nears the microchannel entrance, the interruption of the thermal boundary layer caused by the magnetic source occurs earlier because the thermal boundary is not fully developed.

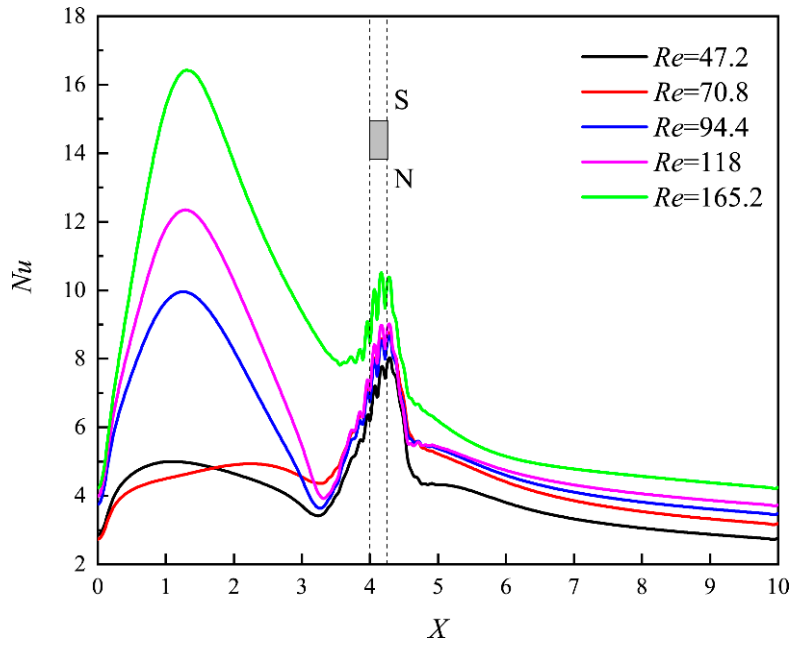

Figure 7. Influence of the Reynolds number on Nu_{loc} at the upper wall for X_i = 4 and R = 1/4.

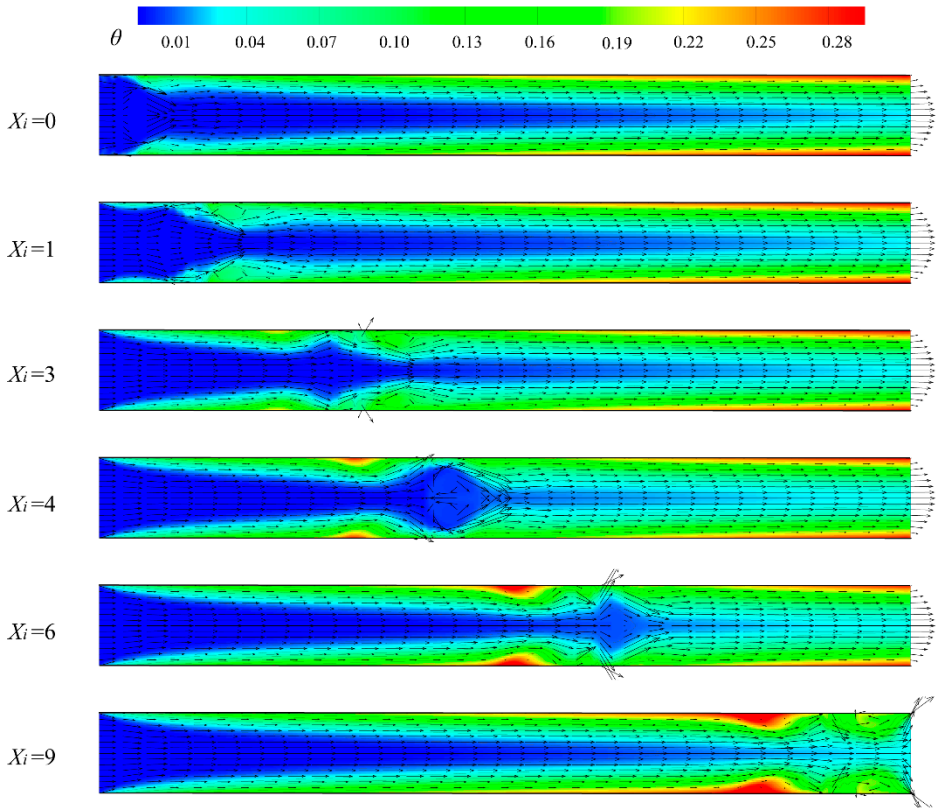

Figure 8. Influence of the magnet position on the velocity field and temperature field in a microchannel for R = 1 and Re = 47.2.

3.3. Effect of Magnet Position (X_i)

Figures 9 and 10 show the influence of magnet position on the temperature and Nusselt number at the upper wall are illustrated for R = 1 and Re = 47.2, respectively. In general, the temperature of the upper wall increases along the length of the microchannel at

different positions of the magnet, and local high and low temperatures will occur near the magnet. The Nu_{loc} decreases with the increase of microchannel length at different magnet positions, and the Nu_{loc} in the entrance section is the largest. This is because the thermal boundary layer in the entrance section has not been fully developed, and there is no space for the front end of the magnet to form a stagnant region. As the parameter X_i increases, the corresponding heat transfer enhancement of the magnet to FHD decreases gradually, and the effect is the smallest at the exit, that is, when X_i = 9.

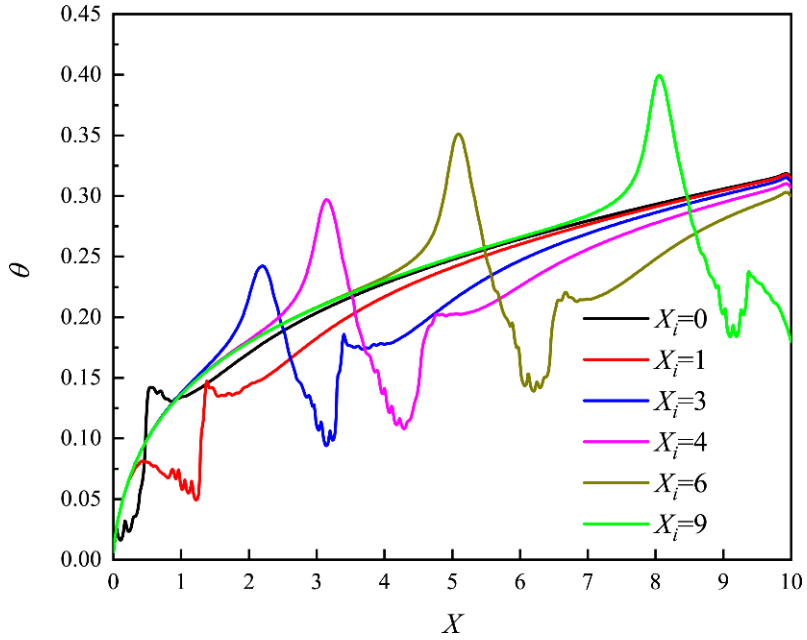

Figure 9. Influence of the magnet position on the temperature at the upper wall for R = 1 and Re = 47.2.

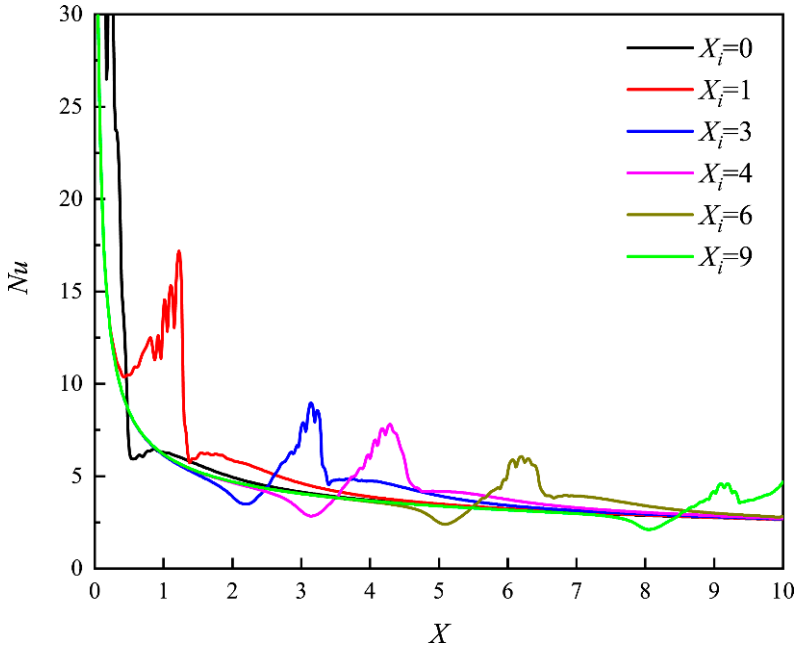

Figure 10. Influence of the magnet position on Nu_{loc} at the upper wall for R = 1 and Re = 47.2.

To understand the influence of magnets on the heat transfer of nanofluid as a whole, Figure 11 shows the effect of permanent magnet positions on the average Nusselt number at the upper wall for Re = 47.2. It can be seen that the magnetic field enhances the heat transfer of nanofluid, and the average Nusselt number increases. The position of the magnet has an important influence on the heat transfer of nanofluid. The average Nusselt number decreases as the magnet position moves backward along the long direction of the microchannel. When the inlet opening R was 1 and 1/4, the average Nusselt number was 5.315 and 4.182, respectively, at X_i = 0.5. Compared with the non-magnetic field, the heat transfer gain increased by 17.2% and 35.2%, respectively.

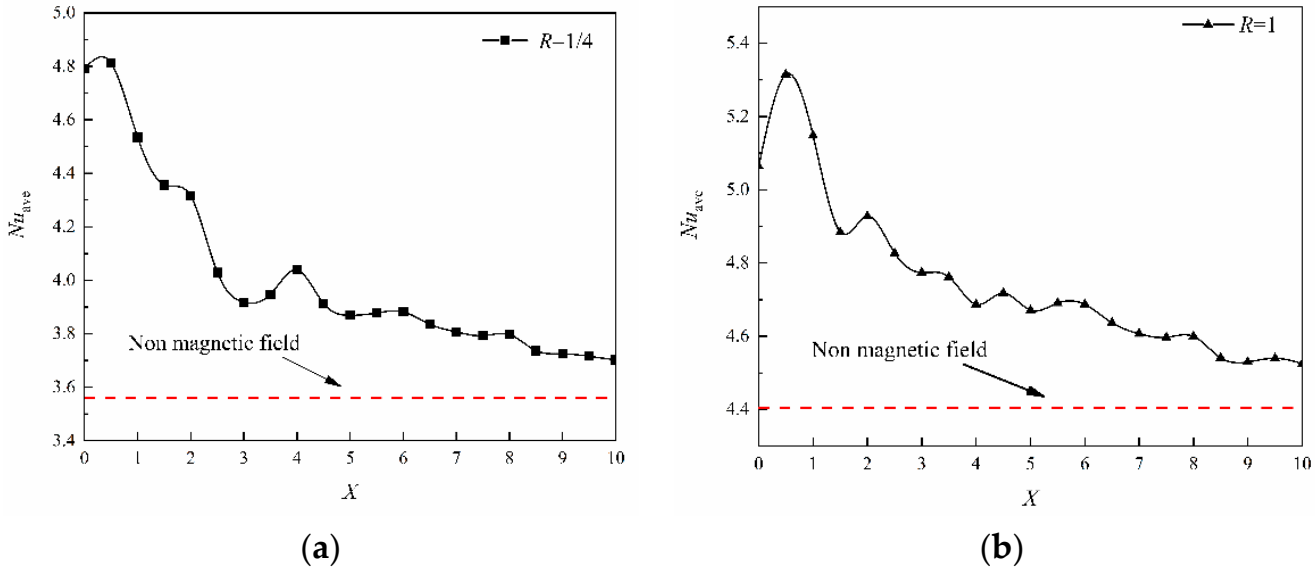

Figure 11. Influence of the permanent magnet positions on the average Nusselt number at the upper wall for Re = 47.2.

4. Conclusions

In the present study, heat transfer and flow characteristics of Fe_3O_4-H_2O nanofluid in a microchannel under the action of magnets are studied. Moreover, the influence of the magnetic field on the flow characteristics and thermal behaviors was studied for different inlet openings, the configuration of permanent magnets and Reynolds number. Based on the obtained results, the main achievements of this study can be summarized as follows:

(1) At high inlet opening, e.g., R = 1, 1/2, 1/4, the nanofluid in the microchannel is symmetrical up and down. When the inlet opening is reduced to R = 1/8, the flow of nanofluid deflects upward to form an asymmetric structure. There are two recirculation zones near the upper and lower walls, and the local high temperature appears near the upper and lower walls at the microchannel entrance. The local high-temperature region at the microchannel entrance increases with the decrease of the inlet opening.

(2) At a low Reynolds number, the closer the magnetic source is to the inlet, the greater the influence on the flow and heat transfer of nanofluid. The influence of magnets on the flow and heat transfer of nanofluid decreases with the increase of Reynolds number. The main factors affecting the flow of nanofluids are magnetic field intensity and Reynolds number. When the magnetic field intensity remains unchanged, the force of magnetic field on nanoparticles decreases with the increase of Reynolds number.

(3) The position of magnets has an important effect on the heat transfer of nanofluid, the average Nusselt number decreases as the magnet position moves backward along the long direction of the microchannel. Compared with the absence of a magnetic field, when the inlet opening R is 1 and 1/4, the heat transfer gain increases by 17.2% and 35.2%, respectively.

Author Contributions: Conceptualization, Y.X. and C.J.; methodology, Y.X.; software, Y.X., P.Z., Z.C. and M.L.; validation, P.Z., Z.C. and M.L.; formal analysis, P.Z. and Z.C.; investigation, Y.X., P.Z. and Z.C.; writing—original draft preparation, Y.X.; writing—review and editing, C.J.; visualization, Y.X. and Z.C.; supervision, C.J.; project administration, C.J.; funding acquisition, C.J. All authors have read and agreed to the published version of the manuscript.

Funding: This research was funded by National Natural Science Foundation of China Grant Numer [11572056].

Institutional Review Board Statement: Not applicable.

Informed Consent Statement: Not applicable.

Data Availability Statement: All the data contains with in the manuscript.

Acknowledgments: The authors thank the financial support of the National Natural Science Foundation of China (No.11572056).

Conflicts of Interest: The authors declare that they have no conflict of interests regarding the publication of this paper.

Appendix A

The Kelvin force can be expressed in the form below [34]:

$$\mathbf{f} = (\mathbf{M}\cdot\nabla)\mathbf{B} \tag{A1}$$

where, $\mathbf{B} = \mu_0(1+\chi)\mathbf{H}$ and $\mathbf{M} = \chi\mathbf{H}$. Consequently, the Kelvin force can be written as the following:

$$\mathbf{f} = \mu_0\chi\mathbf{H}\cdot\nabla((1+\chi)\mathbf{H}) = \frac{1}{2}\mu_0\chi(1+\chi)\nabla(\mathbf{H}\cdot\mathbf{H}) + \mu_0\chi(\mathbf{H}\cdot\nabla\chi)\mathbf{H} \tag{A2}$$

Introducing this Kelvin force to the momentum equation, the ferromagnetic hydrodynamics phenomenon for Fe_3O_4-H_2O nanofluid can be expressed in the form below:

$$\rho_{nf}\mathbf{U}\cdot\nabla\mathbf{U} = -\nabla p + \mu_{nf}\nabla^2\mathbf{U} + \frac{1}{2}\mu_0\chi(1+\chi)\nabla(\mathbf{H}\cdot\mathbf{H}) + \mu_0\chi(\mathbf{H}\cdot\nabla\chi)\mathbf{H} \tag{A3}$$

At the reference state, there is no convection. Accordingly, Equation (A3) can be rewritten in the form below:

$$0 = -\nabla p_0 + \frac{1}{2}\mu_0\chi_0(1+\chi_0)\nabla(\mathbf{H}\cdot\mathbf{H}) \tag{A4}$$

Subtracting Equation (A4) from Equation (A3), yields the following expression:

$$\begin{aligned}\rho_{nf}\mathbf{U}\cdot\nabla\mathbf{U} = {} & -\nabla(p-p_0) + \mu_{nf}\nabla^2\mathbf{U} + \tfrac{1}{2}\mu_0\chi(1+\chi)\nabla(\mathbf{H}\cdot\mathbf{H}) + \mu_0\chi(\mathbf{H}\cdot\nabla\chi)\mathbf{H} \\ & -\tfrac{1}{2}\mu_0\chi_0(1+\chi_0)\nabla(\mathbf{H}\cdot\mathbf{H})\end{aligned} \tag{A5}$$

Based on Curie's law, mass magnetic susceptibility has an adverse correlation with absolute temperature.

$$\chi = \frac{c}{T} \tag{A6}$$

where c is a constant. Applying the Taylor expansion, to χ yields in the following expression:

$$\chi = \chi_0 + \left(\frac{\partial\chi}{\partial T}\right)_i (T-T_i) \approx \chi_0\Big(1-\beta_{nf}(T-T_i)\Big) \tag{A7}$$

$$\nabla\chi = -\chi_0\Big[1+\beta_{nf}(T-T_i)\Big]^{-2}\beta_{nf}\nabla T \approx -\frac{\chi_0}{2}\Big[1-2\beta_{nf}(T-T_i)\Big]\beta_{nf}\nabla T \tag{A8}$$

and

$$\chi^2 \;=\; \chi_0^2\Big[1+\beta_{nf}(T-T_i)\Big]^{-2} \approx \chi_0^2\Big[1-2\beta_{nf}(T-T_i)\Big] \tag{A9}$$

Substituting Equations (A7)–(A9) into Equation (A5), we have

$$\begin{gathered}\rho_{nf}\mathbf{U}\cdot\nabla\mathbf{U} \;=\; -\nabla p^* + \mu_{nf}\nabla^2\mathbf{U} - \tfrac{1}{2}\mu_0\chi_0\beta_{nf}(T-T_i)\nabla(\mathbf{H}\cdot\mathbf{H}) \\ -\mu_0\chi_0^2\beta_{nf}(T-T_i)\nabla(\mathbf{H}\cdot\mathbf{H}) + \mu_0\chi_0^2\beta_{nf}\Big[1-3\beta_{nf}(T-T_i)\Big](\mathbf{H}\cdot\nabla T)\mathbf{H}\end{gathered} \tag{A10}$$

Considering the magnitude difference between individual terms, Equation (A10) can be further simplified. The last term on the right-hand side can be simplified to $\mu_0\chi_0^2\beta_{nf}(\mathbf{H}\cdot\nabla T)\mathbf{H}$.

Therefore, the momentum equation is simplified to the form

$$\begin{gathered}\rho_{nf}\mathbf{U}\cdot\nabla\mathbf{U} \;=\; -\nabla p^* + \mu_{nf}\nabla^2\mathbf{U} - \tfrac{1}{2}\mu_0\chi_0\beta_{nf}(T-T_i)\nabla(\mathbf{H}\cdot\mathbf{H}) \\ -\mu_0\chi_0^2\beta_{nf}(T-T_i)\nabla(\mathbf{H}\cdot\mathbf{H}) + \mu_0\chi_0^2\beta_{nf}(\mathbf{H}\cdot\nabla T)\mathbf{H}\end{gathered} \tag{A11}$$

Equation (A11) along the x direction and y direction can be expressed as follows:

$$\begin{gathered}\rho_{nf}\Big(u\tfrac{\partial u}{\partial x}+v\tfrac{\partial u}{\partial y}\Big) \;=\; -\tfrac{\partial p^*}{\partial x} + \mu_{nf}\Big(\tfrac{\partial^2 u}{\partial x^2}+\tfrac{\partial^2 u}{\partial y^2}\Big) - \tfrac{1}{2}\mu_0\chi_0\beta_{nf}(T-T_i)\tfrac{\partial \mathbf{H}^2}{\partial x} \\ -\mu_0\chi_0^2\beta_{nf}(T-T_i)\tfrac{\partial \mathbf{H}^2}{\partial x} - \mu_0\chi_0^2\beta_{nf}\Big(H_x\tfrac{\partial T}{\partial x}+H_y\tfrac{\partial T}{\partial y}\Big)H_x\end{gathered} \tag{A12}$$

$$\begin{gathered}\rho_{nf}\Big(u\tfrac{\partial v}{\partial x}+v\tfrac{\partial v}{\partial y}\Big) \;=\; -\tfrac{\partial p^*}{\partial y} + \mu_{nf}\Big(\tfrac{\partial^2 v}{\partial x^2}+\tfrac{\partial^2 v}{\partial y^2}\Big) - \tfrac{1}{2}\mu_0\chi_0\beta_{nf}(T-T_i)\tfrac{\partial \mathbf{H}^2}{\partial y} \\ -\mu_0\chi_0^2\beta_{nf}(T-T_i)\tfrac{\partial \mathbf{H}^2}{\partial y} - \mu_0\chi_0^2\beta_{nf}\Big(H_x\tfrac{\partial T}{\partial x}+H_y\tfrac{\partial T}{\partial y}\Big)H_y\end{gathered} \tag{A13}$$

Dimensionless form of these equations is presented in Equations (21) and (22).

Appendix B. Nomenclature Table

Symbol	Unit	Description
B	T	magnetic induction
Br	T	residual flux density of permanent magnet
C_p	J/kg·K	specific heat at constant pressure
d	mm	height of jet inlet
d_p	m	nanoparticle diameter of the base fluid
D_B	m/s^2	Brownian diffusion coefficient
D_T	m/s^2	thermophoresis diffusion coefficient
f	N/m^3	Kelvin body force
H	A/m	magnetic field strength
h	mm	channel height
h_1	mm	width of magnet
h_2	mm	distance between permanent magnet and microchannel
k	W/m·K	thermal conductivity
k_B	J/K	Boltzmann's constant
l	mm	microchannel length
l_1	mm	length of magnet
M	A/m	magnetization
m	A·m	magnetic moment (strength) per unit length of line dipole
p	Pa	pressure
P		dimensionless pressure
Nu		Nusselt number
Pr		Prandtl number
q	W/cm^2	heat flux density
R		opening ratio
Re		Reynolds number
T	K	temperature
T_c	K	Curie temperature

u, v	m/s	velocity components
U	m/s	velocity vector
x, y	mm	axial and transverse coordinate
x_i	mm	position of permanent magnet
X_i		dimensionless position of permanent magnet
Greek symbols		
θ		dimensionless temperature
μ	N·s/m^2	dynamic viscosity
ρ	kg/m^3	density
ϕ		volume fraction of nanoparticles
χ		magnetic susceptibility at operating temperature
χ_0		magnetic susceptibility at reference temperature
μ_0	T·m/A	magnetic permeability of vacuum
β	K^{-1}	volume expansion coefficient
γ		Kelvin body force number
Subscripts		
f		base fluid
i		inlet
lower		lower wall
nf		nanofluid
p		nanoparticle
upper		upper wall
w		walls
0		reference state
loc		local

References

1. He, Z.; Yan, Y.; Zhang, Z. Thermal management and temperature uniformity enhancement of electronic devices by micro heat sinks: A review. *Energy* **2021**, *216*, 119223. [CrossRef]
2. Rostamian, F.; Etesami, N.; Haghgoo, M. Management of electronic board temperature using heat sink containing pure and microencapsulated phase change materials. *Int. Commun. Heat Mass Transf.* **2021**, *126*, 105407. [CrossRef]
3. Alhusseny, A.; Al-Aabidy, Q.; Al-Zurfi, N.; Nasser, A.; Aljanabi, M. Cooling of high-performance electronic equipment using graphite foam heat sinks. *Appl. Therm. Eng.* **2021**, *191*, 116844. [CrossRef]
4. Kannan, K.G.; Kamatchi, R. Experimental investigation on thermosyphon aid phase change material heat exchanger for electronic cooling applications. *J. Energy Storage* **2021**, *39*, 102649. [CrossRef]
5. Siricharoenpanich, A.; Wiriyasart, S.; Naphon, P. Study on the thermal dissipation performance of GPU cooling system with nanofluid as coolant. *Case Stud. Therm. Eng.* **2021**, *25*, 100904. [CrossRef]
6. Ghasemi, S.E.; Ranjbar, A.; Hosseini, S.M.J. Experimental evaluation of cooling performance of circular heat sinks for heat dissipation from electronic chips using nanofluid. *Mech. Res. Commun.* **2017**, *84*, 85–89. [CrossRef]
7. Keshavarz, F.; Lavasani, A.M.; Bayat, H. Numerical analysis of the effect of nanofluid and fin distribution density on thermal and hydraulic performance of a heat sink with drop-shaped micropin fins. *J. Therm. Anal. Calorim.* **2019**, *135*, 1211–1228. [CrossRef]
8. Buongiorno, J. Convective Transport in Nanofluids. *J. Heat Transf.* **2006**, *128*, 240–250. [CrossRef]
9. Corcione, M. Empirical correlating equations for predicting the effective thermal conductivity and dynamic viscosity of nanofluids. *Energy Convers. Manag.* **2011**, *52*, 789–793. [CrossRef]
10. Ekiciler, R.; Muhammet, S.A.Ç.; Arslanb, K. Effect of shape of nanoparticle on heat transfer and entropy generation of nanofluid-jet impingement cooling. *Int. J. Green Energy* **2020**, *17*, 555–567. [CrossRef]
11. Ambreen, T.; Kim, M.-H. Effects of variable particle sizes on hydrothermal characteristics of nanofluids in a microchannel. *Int. J. Heat Mass Transf.* **2018**, *120*, 490–498. [CrossRef]
12. Bowers, J.; Cao, H.; Qiao, G.; Li, Q.; Zhang, G.; Mura, E.; Ding, Y.L. Flow and heat transfer behaviour of nanofluids in microchannels. *Prog. Nat. Sci.* **2018**, *28*, 225–234. [CrossRef]
13. Vijayan, G.; Shantharaman, P.P.; Senthil, R.; Karunakaran, R. Thermal performance analysis of a low volume fraction Al_2O_3 and deionized water nanofluid on solar parabolic trough collector. *J. Therm. Anal. Calorim.* **2020**, 1–10. [CrossRef]
14. Kaya, H.; Ekiciler, R.; Arslan, K. CFD analysis of laminar forced convective heat transfer for TiO_2/water nanofluid in a semi-circular cross-sectioned micro-channel. *J. Therm. Eng.* **2019**, *5*, 123–137.
15. Sheikholeslami, M.; Hayat, T.; Alsaedi, A. Numerical study for external permanent magnets influence on water based nanofluid convective heat transfer. *Int. J. Heat Mass Transf.* **2017**, *106*, 745–755. [CrossRef]
16. Sheikholeslami, M.; Shehzad, S. Numerical analysis of Fe_3O_4–H_2O nanofluid flow in permeable media under the effect of external magnetic source. *Int. J. Heat Mass Transf.* **2018**, *118*, 182–192. [CrossRef]

17. Sheikholeslami, M.; Sheremet, M.A.; Shafee, A.; Tlili, I. Simulation of nanoliquid thermogravitational convection within a porous chamber imposing magnetic and radiation impacts. *Phys. A Stat. Mech. Its Appl.* **2020**, *550*, 124058. [CrossRef]
18. Karami, E.; Rahimi, M.; Azimi, N. Convective heat transfer enhancement in a pitted microchannel by stimulation of magnetic nanoparticles. *Chem. Eng. Process. Process. Intensif.* **2018**, *126*, 156–167. [CrossRef]
19. Cunha, L.H.P.; Siqueira, I.R.; Campos, A.A.R. A numerical study on heat transfer of a ferrofluid flow in a square cavity under simultaneous gravitational and magnetic convection. *Theor. Comput. Fluid Dyn.* **2020**, *34*, 119–132. [CrossRef]
20. Muthukumar, S.; Sureshkumar, S.; Chamkha, A.J.; Muthtamilselvan, M.; Prem, E. Combined MHD convection and thermal radiation of nanofluid in a lid-driven porous enclosure with irregular thermal source on vertical sidewalls. *J. Therm. Anal. Calorim.* **2019**, *138*, 583–596. [CrossRef]
21. Benos, L.T.; Polychronopoulos, N.D.; Mahabaleshwar, U.S.; Lorenzini, G.; Sarris, I.E. Thermal and flow investigation of MHD natural convection in a nanofluid-saturated porous enclosure: An asymptotic analysis. *J. Therm. Anal. Calorim.* **2021**, *143*, 751–765. [CrossRef]
22. Salehpour, A.; Salehi, S.; Salehpour, S.; Ashjaee, M. Thermal and hydrodynamic performances of MHD ferrofluid flow inside a porous channel. *Exp. Therm. Fluid Sci.* **2018**, *90*, 1–13. [CrossRef]
23. Goharkhah, M.; Salarian, A.; Ashjaee, M.; Shahabadi, M. Convective heat transfer characteristics of magnetite nanofluid under the influence of constant and alternating magnetic field. *Powder Technol.* **2015**, *274*, 258–267. [CrossRef]
24. Mehrez, Z.; El Cafsi, A. Heat exchange enhancement of ferrofluid flow into rectangular channel in the presence of a magnetic field. *Appl. Math. Comput.* **2021**, *391*, 125634. [CrossRef]
25. Larimi, M.; Ghanaat, A.; Ramiar, A.; Ranjbar, A. Forced convection heat transfer in a channel under the influence of various non-uniform transverse magnetic field arrangements. *Int. J. Mech. Sci.* **2016**, *118*, 101–112. [CrossRef]
26. Bagherzadeh, S.A.; Jalali, E.; Sarafraz, M.M.; Akbari, O.A.; Karimipour, A.; Goodarzi, M.; Bach, Q.-V. Effects of magnetic field on micro cross jet injection of dispersed nanoparticles in a microchannel. *Int. J. Numer. Methods Heat Fluid Flow* **2020**, *30*, 2683–2704. [CrossRef]
27. Jing, D.; Hu, S.; Hatami, M.; Xiao, Y.; Jia, J. Thermal analysis on a nanofluid-filled rectangular cavity with heated fins of different geometries under magnetic field effects. *J. Therm. Anal. Calorim.* **2019**, *139*, 3577–3588. [CrossRef]
28. Falade, J.; Ukaegbu, J.C.; Egere, A.; Adesanya, S.O. MHD oscillatory flow through a porous channel saturated with porous medium. *Alex. Eng. J.* **2017**, *56*, 147–152. [CrossRef]
29. Sivasankaran, S.; Narrein, K. Influence of geometry and magnetic field on convective flow of nanofluids in trapezoidal microchannel Heat Sink. *IJST-T. Mech. Eng.* **2018**, *44*, 373–382. [CrossRef]
30. Zanella, R.; Nore, C.; Bouillault, F.; Guermond, J.-L.; Mininger, X. Influence of thermomagnetic convection and ferrofluid thermophysical properties on heat transfers in a cylindrical container heated by a solenoid. *J. Magn. Magn. Mater.* **2019**, *469*, 52–63. [CrossRef]
31. Soltanipour, H. Two-phase simulation of magnetic field effect on the ferrofluid forced convection in a pipe considering Brownian diffusion, thermophoresis, and magnetophoresis. *Eur. Phys. J. Plus* **2020**, *135*, 1–23. [CrossRef]
32. Nessab, W.; Kahalerras, H.; Fersadou, B.; Hammoudi, D. Numerical investigation of ferrofluid jet flow and convective heat transfer under the influence of magnetic sources. *Appl. Therm. Eng.* **2019**, *150*, 271–284. [CrossRef]
33. Ranjan, G.; Swarnendu, S.; Ishwar, K. Heat transfer augmentation using a magnetic fluid under the influence of a line dipole. *J. Magn. Magn. Mater.* **2004**, *271*, 63–73.
34. Bashtovoy, V.G.; Berkovsky, B.M.; Vislovich, A.N. *Introduction to Thermomechanics of Magnetic Fluids*; Hemisphere Publishing Corporation: New York, NY, USA, 1998.